

Uncertainty-aware molecular dynamics from Bayesian active learning: Phase Transformations and Thermal Transport in SiC

Boris Kozinsky (✉ bkoz@seas.harvard.edu)

Harvard University <https://orcid.org/0000-0002-0638-539X>

Yu Xie

Harvard University <https://orcid.org/0000-0002-0088-5123>

Jonathan Vandermause

Harvard University <https://orcid.org/0000-0001-5559-3147>

Senja Ramakers

Corporate Sector Research and Advance Engineering, Robert Bosch GmbH, Renningen

Nakib Protik

ICN2 <https://orcid.org/0000-0001-7839-9881>

Anders Johansson

Harvard University

Article

Keywords:

Posted Date: June 2nd, 2022

DOI: <https://doi.org/10.21203/rs.3.rs-1606203/v1>

License: © ⓘ This work is licensed under a Creative Commons Attribution 4.0 International License.

[Read Full License](#)

1 **Uncertainty-aware molecular dynamics from Bayesian active**
2 **learning: Phase Transformations and Thermal Transport in SiC**

3 Yu Xie,^{1,*} Jonathan Vandermause,^{1,2} Senja Ramakers,^{3,4}

4 Nakib H. Protik,¹ Anders Johansson,¹ and Boris Kozinsky^{1,5,†}

5 ¹*John A. Paulson School of Engineering and Applied Sciences, Harvard University*

6 ²*Department of Physics, Harvard University*

7 ³*Corporate Sector Research and Advance Engineering, Robert Bosch GmbH, Renningen*

8 ⁴*Interdisciplinary Centre for Advanced Materials Simulation, Ruhr-Universität Bochum*

9 ⁵*Robert Bosch LLC, Research and Technology Center*

 Abstract

Machine learning interatomic force fields are promising for combining high computational efficiency and accuracy in modeling quantum interactions and simulating atomic level processes. Active learning methods have been recently developed to train force fields efficiently and automatically. Among them, Bayesian active learning utilizes principled uncertainty quantification to make data acquisition decisions. In this work, we present an efficient Bayesian active learning workflow, where the force field is constructed from a sparse Gaussian process regression model based on atomic cluster expansion descriptors. To circumvent the high computational cost of the sparse Gaussian process uncertainty calculation, we formulate a high-performance approximate mapping of the uncertainty and demonstrate a speedup of several orders of magnitude. As an application, we train a model for silicon carbide (SiC), a wide-gap semiconductor with complex polymorphic structure and diverse technological applications in power electronics, nuclear physics and astronomy. We show that the high pressure phase transformation is accurately captured by the autonomous active learning workflow. The trained force field shows excellent agreement with both *ab initio* calculations and experimental measurements, and outperforms existing empirical models on vibrational and thermal properties. The active learning workflow readily generalizes to a wide range of systems and accelerates computational understanding and design.

10 I. INTRODUCTION

11 Machine learning interatomic force fields have recently emerged as powerful tools in mod-
12 eling interatomic interactions. They are capable of reaching near-quantum accuracy while
13 being orders of magnitude faster than *ab initio* methods¹⁻⁷. While predictions of energies
14 and forces with machine learning force fields are much faster than with *ab initio* methods,
15 the process of generating the reference data and training the model can be computationally
16 expensive, for two reasons. First, relevant training data is typically generated by *ab ini-*
17 *tio* molecular dynamics, where each step consists of an expensive density functional theory
18 (DFT) calculation. Second, a large training set is often required for sufficient sampling of
19 important but rare events that occur in diffusion, reaction or phase transformation scenarios,
20 and the cost of optimizing a model increases with the size of the training set.

21 Recently, efficient active learning schemes have been demonstrated where molecular dy-
22 namics (MD) is driven by the machine learning force field, and only configurations satisfying
23 certain acquisition criteria^{6,8-13} are computed with accurate but expensive DFT calculations
24 and added to the training set. Among them, the FLARE⁶ framework utilizes principled
25 Gaussian process (GP) uncertainties to construct a Bayesian force field (BFF), a force field
26 equipped with internal uncertainty quantification from Bayesian inference, enabling a fully
27 autonomous active learning workflow.

28 The cost of prediction of conventional GP models scales linearly with the training set
29 size, making it computationally expensive for large data sets. The sparse Gaussian process
30 (SGP) approach selects a set of representative atomic environments from the entire training
31 set to build an approximate model, which can scale to a larger training data set, but still
32 suffers from the linear scaling of the inference cost. To address this issue, it was noticed that
33 for the particular structure of the squared exponential 2+3-body kernel, it is possible to
34 map the mean prediction of a trained model onto an equivalent low-dimensional parametric
35 model^{6,14,15} without any loss of accuracy. It was subsequently shown that the evaluation of
36 the variance can also be mapped onto a low-dimensional model, achieving a dramatically
37 accelerated uncertainty-aware BFF¹⁶. In the case of inner-product kernels with many-body
38 descriptors, the prediction of the mean can be mapped exactly onto a constant-cost model
39 via reorganization of the summation in the mathematical expression for the SGP mean
40 calculation¹⁷. This allows for very efficient evaluation of the model forces, energies and

41 stresses, but does not address the cost of evaluating uncertainties in such many-body models.

42 In this work, we present a method to map the variance of SGP models with inner product
43 kernels. This advance enables large-scale uncertainty aware MD and overcome the linear
44 scaling issue of SGPs. Building on this approach, we achieve a significant acceleration of the
45 Bayesian active learning (BAL) workflow and integrate it with Large-scale Atomic/Molecular
46 Massively Parallel Simulator (LAMMPS)¹⁸. Bayesian force fields are implemented within the
47 LAMMPS MD engine, such that both forces and uncertainties for each atomic configuration
48 are quantified at computational cost independent of the training set size.

49 As a demonstration of the accelerated autonomous workflow, we train an uncertainty-
50 aware many-body BFF for silicon carbide (SiC) on its several polymorphs and phases. SiC is
51 a wide-gap semiconductor with diverse applications ranging from efficient power electronics
52 to nuclear physics and astronomy. Recently, it has attracted attention due to the long
53 spin coherence times of point defects under ambient conditions^{19–31}, making it promising
54 for spin-optical interfaces for quantum computing and quantum information technologies.
55 The phase transition of SiC under extreme conditions is relevant for studying carbon-rich
56 exoplanets³² and superhard materials³³, where the transition from the zinc blende (3C)
57 to the rock salt (RS) phase is observed at high pressure from experiments^{32,34–39} and *ab*
58 *initio* calculations^{40–47}. Empirical potentials such as Tersoff^{48,49}, Vashishta^{50,51}, MEAM⁵²,
59 and Gao-Weber⁵³ have been developed and applied in large-scale simulations for different
60 purposes. However, empirical analytical potentials are limited in descriptive complexity,
61 and hence accuracy, and require intensive human effort to select training configurations and
62 to train. Machine learning approaches have allowed for highly over-parameterized or non-
63 parametric models to be trained on a wide range of structures and phases^{7,54–57}. Recently,
64 neural network potentials were trained for SiC to study dielectric spectra⁵⁸ and thermal
65 transport properties⁵⁹, but they do not capture high-pressure phase transitions.

66 In the present work, we deploy the accelerated autonomous BAL workflow to the high-
67 pressure phase transition of SiC, and demonstrate that the transition process can be captured
68 by the uncertainty quantification of the BFF. Then the BFF is used to perform large-scale
69 MD simulations, and compute vibrational and thermal transport properties of different
70 phases. The FLARE BFF shows excellent agreement with *ab-initio* calculations⁶⁰ and ex-
71 perimental measurements, and significantly outperforms available empirical potentials in
72 terms of accuracy, while retaining comparable computational efficiency.

73 II. RESULTS AND DISCUSSIONS

74 A. Accelerated Bayesian Active Learning Workflow

75 Directly using *ab initio* MD to generate a sufficiently diverse training set for machine
76 learning force fields is expensive and time consuming, and may still miss higher-energy
77 configurations important for rare transformation phenomena. Here, we develop an active
78 learning workflow, where MD is instead driven by the much faster surrogate FLARE many-
79 body BFF. During the MD simulation, the model uses its internal uncertainty quantification,
80 deciding to call DFT only when the model encounters atomic configurations with uncertainty
81 above a chosen threshold. Within this framework, a much smaller number of DFT calls are
82 needed, which greatly reduces the training time and increases the efficiency of phase space
83 exploration. Active learning of interatomic force fields has recently been demonstrated using
84 the FLARE method⁶, where GP regression is used for force and uncertainty predictions
85 using 2+3 body kernels for comparing local atomic environments in the training and test
86 structures. The cost of GP prediction, which normally scales linearly with the training set
87 size in GP, can be dramatically reduced by a lossless mapping of the GP model onto a spline
88 model^{6,14} that is evaluated in constant time and allows for modeling dynamics of systems
89 with millions of atoms¹⁶.

90 In this work, we extend the formalism of efficient lossless mapping to include uncertainty
91 of many-body SGP models. Specifically, we implement mapped SGP variance to enable
92 efficient uncertainty quantification and achieve large-scale MD simulations by interfacing
93 the Bayesian active learning algorithm with LAMMPS. The mappings of the forces and
94 uncertainty overcome the scaling with the training set size of the computational cost of SGP
95 regression, resulting in a significant acceleration of the training process in comparison with
96 using the full SGP¹⁷.

97 We illustrate our active learning workflow in Fig. 1a. Starting from a SGP model with a
98 small initial training set, we map both prediction mean and variance into quadratic models
99 to obtain an efficient BFF (details are discussed in *Methods*). With the mapped SGP force
100 field, MD simulation runs in LAMMPS with uncertainty associated with the local energy
101 assigned to each atom in a configuration at each time step. The MD simulation is interrupted
102 once there are atoms whose uncertainties are above the threshold. Then DFT is used to

103 compute energy, forces and stress for the high-uncertainty configurations. The training set
 104 is augmented with the newly acquired DFT data, the SGP model is retrained and mapped,
 105 and the MD simulation continues with the updated model.

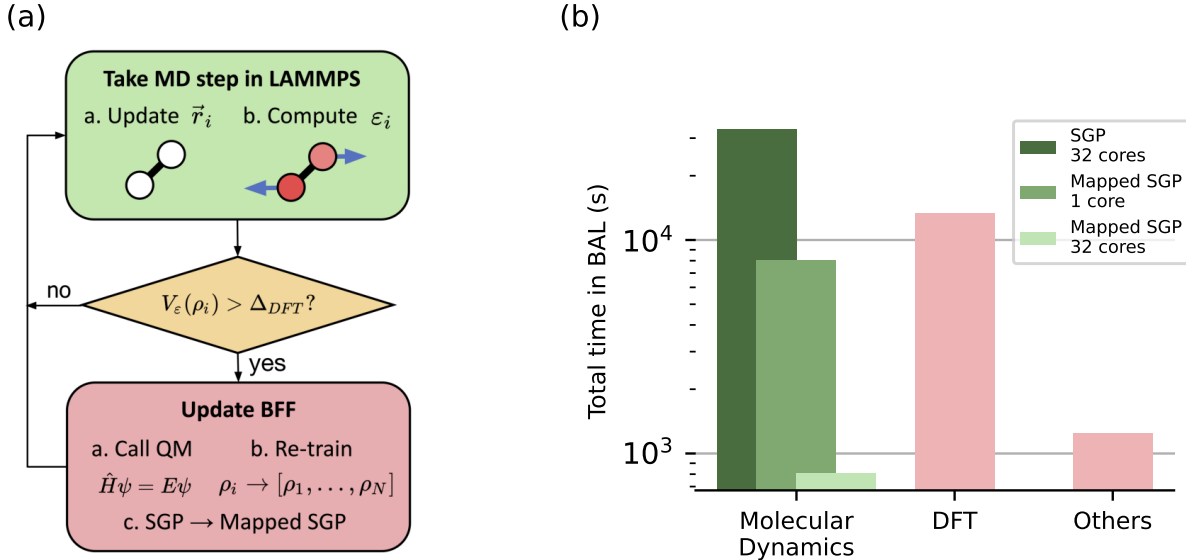


FIG. 1. Workflow and performance. a. Bayesian active learning (BAL) workflow with LAMMPS. It closely follows our previous work¹⁷, with the key addition that the SGP uncertainties are now mapped and therefore much cheaper, and the MD part of the training can be done within LAMMPS. b. Time profiling of the BAL workflow with a system of 72 atoms and 100,000 MD time steps. The MD is greatly accelerated using mapped forces and uncertainty compared to sparse GP. “Others” includes time consumed outside of MD and DFT, e.g. adding training data to SGP and optimizing hyperparameters.

106 To illustrate the acceleration of active learning workflow with mapped forces and variance
 107 compared to that with the SGP model, we deploy a single active learning run of bulk 4H-SiC
 108 system and show the performance of each part of the workflow in Fig. 1b. The SGP BAL
 109 workflow collected 14 frames with 72 atoms each, with 10 representative sparse environments
 110 selected per frame. The time step of the MD is 0.1 fs, and the MD runs for a total time of 10
 111 ps. If the model is not mapped, the computational cost of MD with the SGP dominates the
 112 BAL procedure. When the mapped force field and variances are used, the computational cost
 113 is significantly reduced. The FLARE BFF achieves 0.76 ms·CPU/step/atom in LAMMPS
 114 MD, which includes uncertainty quantification, and is comparable in speed to empirical

115 interatomic potentials such as ReaxFF⁶¹. With mapped uncertainties, the DFT calculations
116 become the dominant part from Fig. 1b, i.e. the computational time for BAL is determined
117 by the number of DFT calls. We also note that the SGP model used for timing here has a
118 small training set of 14 frames, and the computational cost of prediction grows linearly with
119 training set size. It is worth emphasizing that after mapping, the prediction of model forces,
120 energies, and stresses, and their variances is independent of the training set size. Therefore,
121 the speedup versus the SGP model is more pronounced as more training data are collected.

122 B. Bayesian Force Field of SiC for High Pressure Phase Transition

123 In this work, we demonstrate the accelerated BAL procedure by training a mapped
124 uncertainty-aware Bayesian force field to describe the phase transition of SiC at high pres-
125 sure. We set up compressive and decompressive MD simulations at temperatures of 300
126 K and 2000 K for on-the-fly training simultaneously, where each SGP model is initialized
127 with an empty training set. The complete training set information is in the Table 2 of the
128 supplementary material.

129 The compressive MD starts with the 2H, 4H, 6H, and 3C polytypes that are stable at
130 low pressure, and the pressure is increased by 30 GPa every 50 ps. The decompressive MD
131 starts with the RS phase at 200 GPa, and the pressure is decreased by 20 GPa every 50 ps.
132 The training data are collected by the BAL workflow shown in Fig. 1. Fig. 2a shows the
133 system volume and relative uncertainty, i.e. the ratio between the uncertainty of the current
134 frame and the average uncertainty of the training data set (see details in supplementary
135 materials⁶²). In the compressive (decompressive) MD, when the transition happens, the
136 volume decreases (increases) rapidly and the uncertainty spikes, since the model has never
137 seen the transition state or the RS (3C) phase before. The post-transition high-pressure
138 structure of the compression run has 6-fold (4-fold) coordination corresponding to the RS
139 (3C) phase, and the transition is observed at 300 GPa (0 GPa) at room temperature. The
140 difference of the transition pressures between the compressive and decompressive simulations
141 is caused by nucleation-driven hysteresis. After the on-the-fly training is done, the training
142 data from compressive and decompressive MD are combined to train a master force field
143 for SiC, such that different phases at different pressures are covered by our force field. In
144 the supplementary materials⁶², we demonstrate the accuracy of our force field on cohesive

145 energy and elastic constants in comparison with DFT.

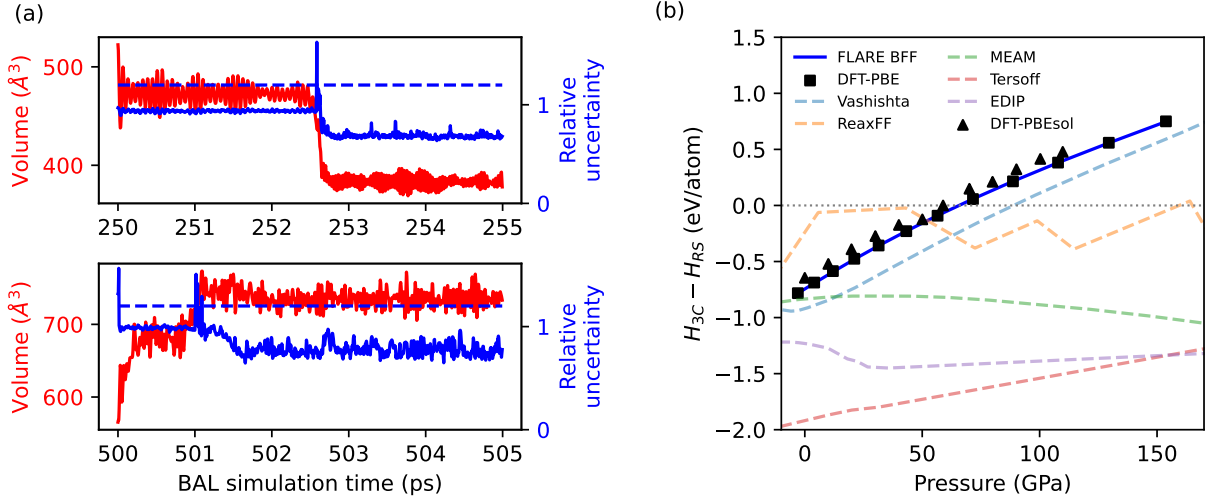


FIG. 2. Phase transition simulation with FLARE BFF and enthalpy calculations. a. A 5 ps segment of the whole training trajectory where the 3C-RS phase transition is captured during the compressive (decompressive) on-the-fly active learning, the volume decreases (increases), and the model uncertainty spikes in the transition state. The uncertainty threshold is shown as the blue dashed line. DFT is called, and new training data is added to the model when the relative uncertainty exceeds the threshold. b. Enthalpy difference predictions from DFT (PBE, PBEsol⁴²), FLARE BFF and existing empirical potentials^{48,50,52,61,63} at pressures from 0 to 150 GPa. The crossing with the dotted zero line gives the transition pressure predicted by enthalpy.

146 Using the mapped master force field, the phase transition pressure (at zero temperature)
 147 can be obtained from the enthalpy $H = E_{\text{total}} + PV$ of the different phases. At low pressure,
 148 the RS phase has higher enthalpy than 3C. With the pressure increased above 65 GPa, the
 149 enthalpy of RS phase becomes lower than 3C. As shown in Fig.2, empirical potentials such as
 150 ReaxFF⁶¹, MEAM⁵², Tersoff⁴⁸ and EDIP⁶³ produce qualitatively incorrect enthalpy curves,
 151 likely because they are trained only at low pressures. The Vashishta potential is the only
 152 one trained on the high pressure 3C-RS phase transition⁵⁰ and presents a consistent scaling
 153 of enthalpy with pressures qualitatively, but it significantly overestimates the transition
 154 pressure at 90 GPa compared to DFT. FLARE BFF achieves an excellent agreement with
 155 the *ab initio* (DFT-PBE) enthalpy predictions, with both methods yielding 65 GPa. We
 156 note that our PBE value is consistent with previous first-principles calculations such as
 157 66.6(LDA)⁴⁰ and 58(PBEsol)⁴².

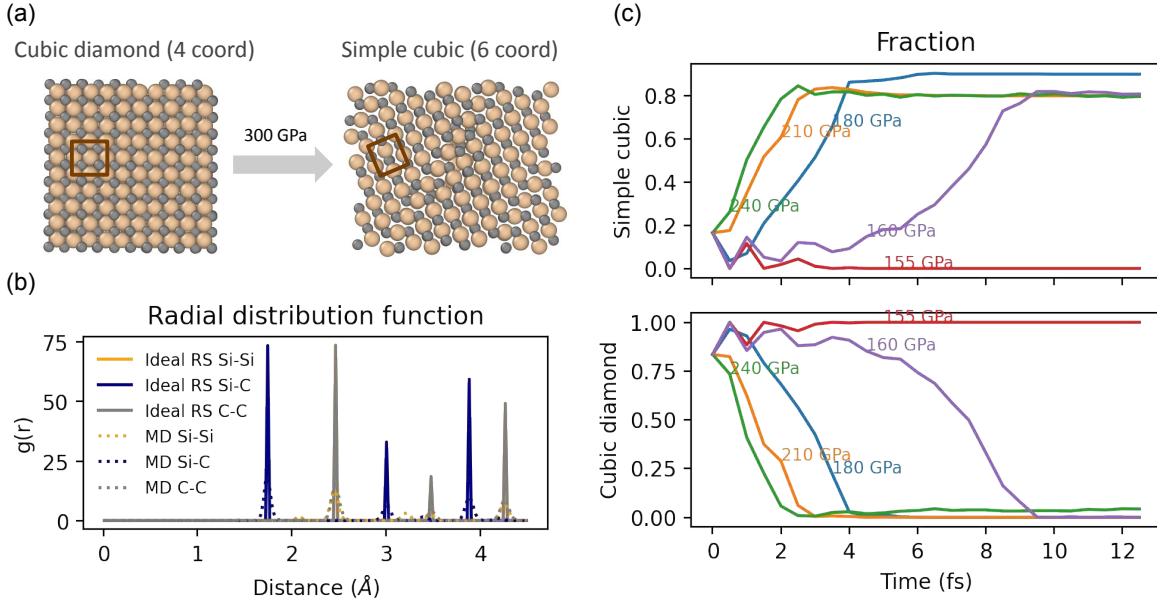


FIG. 3. a. Large-scale MD with 1000 atoms for the 3C-RS phase transition after the training of FLARE BFF is finished. The transition is observed at 300 GPa at room temperature in MD. b. The radial distribution function of the final structure after transition in the MD, compared with the perfect RS crystal lattice, indicating the final configuration is in the RS phase. c. The fraction of simple cubic (RS) and cubic diamond (3C, zinc-blende) atomic environments from the phase boundary evolution at different pressures.

158 Next we run a large-scale MD simulation with 1000 atoms for 500 ps at the temperature
 159 of 300 K. The NPT ensemble is used, and the pressure is increased by 30 GPa every 50 ps.
 160 At 300 GPa, the phase transition is observed from 4-fold coordination to 6-fold, as shown in
 161 Fig.3b. The final 6-fold coordinated structure has radial distribution function as shown in
 162 Fig.3c. The highest C-C, C-Si, Si-Si peaks match the perfect RS structure, confirming that
 163 the final structure is in the rock salt phase.

164 As in the smaller training simulations, the nucleation-controlled hysteresis caused the
 165 transition pressure (300 GPa) to be much higher than in experimental measurements (50-150
 166 GPa)^{32,34,35}. To eliminate the nucleation barrier, we start our simulation with a configuration
 167 where the 3C and RS phases coexist, separated by a phase boundary, and evolve differently
 168 as a function of pressures. It is worth noting that such large scale two-phase simulations
 169 are enabled by the efficient force field and would not be possible to perform with DFT.

170 To recognize simple cubic (RS) and cubic diamond (3C, zinc-blende) environments, we use
 171 polyhedral template matching⁶⁴ in OVITO⁶⁵. The time evolution of the fractions of simple
 172 cubic and cubic diamond atomic environments is shown in Fig. 3c. The phase boundary
 173 evolves quickly within 10 fs. When pressure is greater than 160 GPa, the phase boundary
 174 evolves to RS phase, while below 155 GPa it evolves to 3C phase, which indicates the phase
 175 transition pressure is located between 155-160 GPa at the temperature of 300 K.

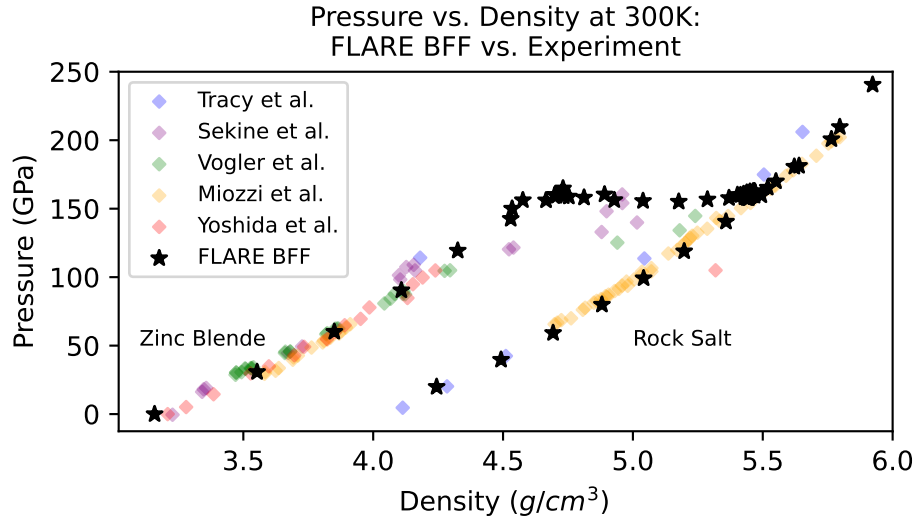


FIG. 4. The density-pressure relation from experimental measurements^{32,34-37} and MD simulations from FLARE BFF.

176 A number of experiments have measured the density-pressure relations of zinc blende
 177 (3C) and rock salt at room temperature^{32,34-37}. As shown in Fig. 4, the equation of state
 178 shows two parallel density-pressure curves, where the one with lower density is associated
 179 with the zinc-blende phase, and the other one with the rock salt phase. The pressures and
 180 corresponding densities at room temperature are extracted from the MD trajectories, and the
 181 equation of state is plotted to compare with the experimental measurements. FLARE BFF
 182 accurately agrees with the experimental measurements for both phases. For the transition
 183 state, there are not many experimental data points available, and the measurements can be
 184 affected by the quality of the sample, but the FLARE BFF still shows good agreement with
 185 the measured data points.

186 C. Vibrational and Thermal Transport Properties

187 To validate that the FLARE BFF gives accurate predictions of thermal properties, we
188 investigate the phonon dispersions and thermal conductivities of the different polytypes
189 and phases of SiC. The phonon dispersions are computed using Phonopy⁶⁶. As shown in
190 Fig. 5, FLARE BFF produces phonon dispersions in close agreement with both DFT and
191 experiments^{67–70} for both the low pressure polytypes and the high pressure rock salt phase
192 at 200 GPa. While in the optical branches the FLARE BFF prediction shows minor discrep-
193 ancies with DFT at the highest frequencies, the phonon density of states (DOS) presents
194 good agreement. In particular, FLARE BFF captures the peak at 23 THz corresponding
195 to a number of degenerate optical branches. Existing empirical potentials are much less
196 accurate than FLARE BFF by comparing the phonon DOS in Fig. 5. We note that the SiC
197 crystals are polarized by atomic displacements and the generated macroscopic field induces
198 an LO-TO splitting near Γ point. The contribution from the polarization should be included
199 through non-analytical correction (NAC)^{66,71}, and the first principle calculation with NAC
200 is discussed in Ref.⁷². However, since FLARE BFF model does not contain charges and
201 polarization, the NAC term is not considered. Thus, our comparison is made between the
202 FLARE BFF and DFT without NAC. The lack of NAC accounts for the disagreement in
203 the high frequencies of the optical bands of 2H DFT phonon (Fig. 5) with experimental
204 measurements near Γ point.

205 Having confirmed the accuracy of the 2nd order force constants by the phonon dispersion
206 calculations, we then compute the thermal conductivity within the Boltzmann transport
207 equation (BTE) formalism. The 2nd and 3rd order force constants are computed using
208 the Phono3py⁷³ code, and then used in the Phoebe⁷⁴ transport code to evaluate thermal
209 conductivity with the iterative BTE solver⁷⁵. In supplementary materials⁶², we verify that
210 the exclusion of the non-analytic correction does not have a significant effect on the thermal
211 conductivity values. Fig. 5 presents the thermal conductivities of the zinc blende phase
212 at 0 GPa and the rock salt phase at 200 GPa as a function of temperature. The FLARE
213 BFF results are in good agreement with the DFT-derived thermal conductivity for both zinc
214 blende and rock salt phases. The thermal conductivity of zinc blende phase computed from
215 DFT and FLARE BFF is also in excellent agreement with experimental measurements^{76–79}.
216 For the high-pressure rock salt phase, the thermal conductivity has not been previously

217 computed or measured to the best of our knowledge. Therefore, our calculation provides a
 218 prediction that awaits experimental verification in the future.

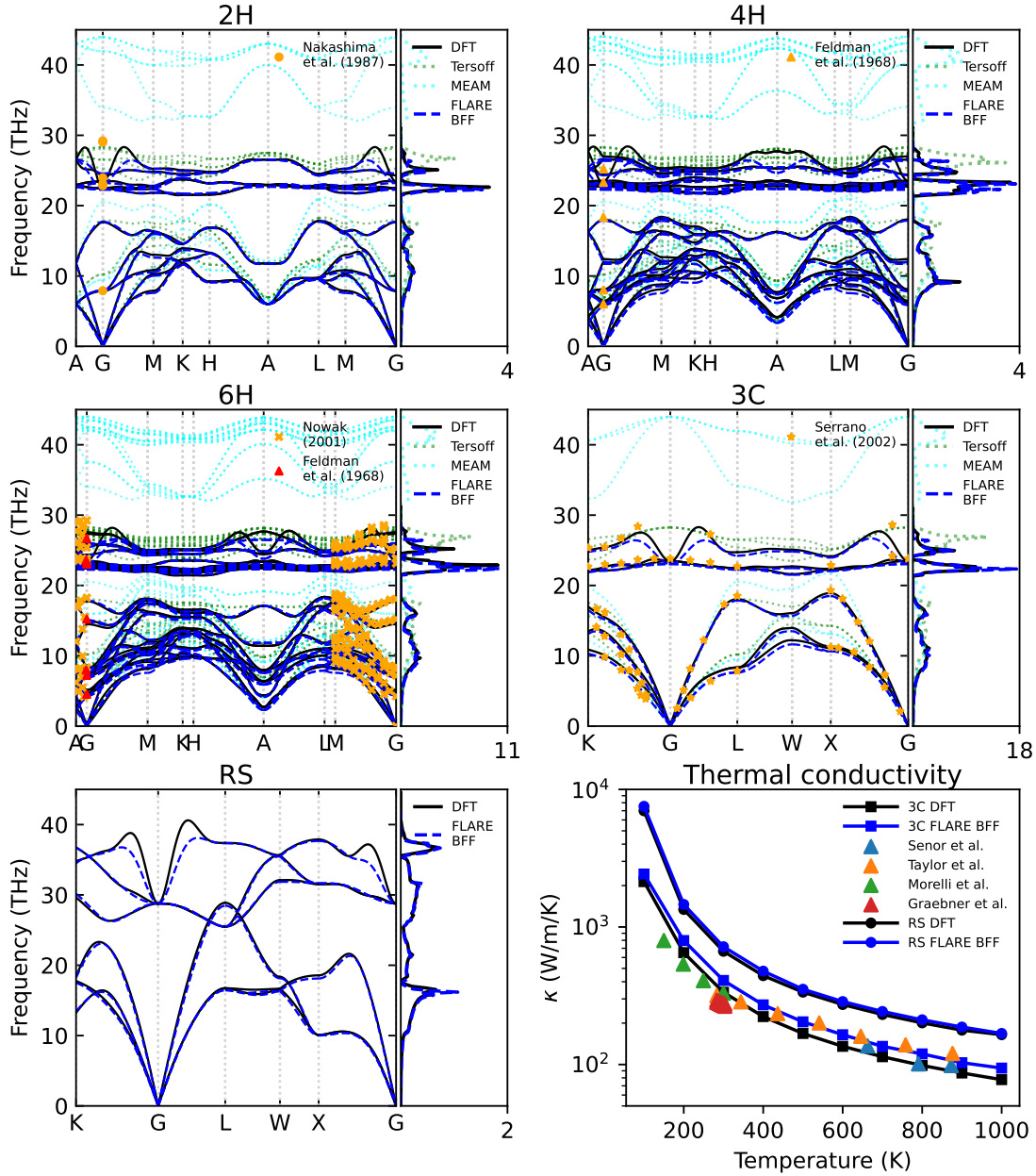


FIG. 5. Phonon dispersions and phonon density of states of different polytypes from experimental measurements^{67–70}, and FLARE BFF and DFT calculations. Lower right: Thermal conductivity of 3C-SiC at 0 GPa and RS phase at 200 GPa with temperatures from 100 to 1000 K, from DFT and FLARE BFF calculations, and the experimental measurements^{76–79} are for 3C-SiC.

219 **III. DISCUSSION**

220 In this work we develop a BFF that maps both the mean predictions and uncertainties
221 of SGP models for many-body interatomic force fields. The mapping procedure overcomes
222 the linear scaling issue of SGPs and results in near-quantum accuracy, while retaining com-
223 putational cost comparable to empirical interatomic potentials such as ReaxFF. The effi-
224 cient uncertainty-aware BFF model forms the basis for the construction of an accelerated
225 autonomous BAL workflow that is coupled with the LAMMPS MD engine and enables
226 large-scale parallel MD simulations. The key improvement with respect to previous meth-
227 ods is the ability of the many-body model to efficiently calculate forces and uncertainties at
228 comparable computational cost.

229 As a demonstration of the ability of this method to capture and learn subtle interac-
230 tions driving phase transformations on-the-fly, we use the BAL workflow to train a BFF
231 for SiC on several common polytypes and phases. The zinc-blende to rock-salt transition
232 is captured in both the active learning and the large-scale simulation, facilitated by the
233 model uncertainty. FLARE BFF is shown to have excellent agreement with DFT for the
234 enthalpy prediction in a wide range of pressure values. The BFF model is readily employed
235 to perform a large-scale MD of the phase boundary evolution, which allows for reliable iden-
236 tification of the transition pressure at room temperature to be located at 155-160 GPa. The
237 density-pressure relation predicted by FLARE BFF agrees very well with experimental mea-
238 surements. We also find close agreement for phonon dispersions and thermal conductivities
239 of several SiC phases, as compared with DFT calculations and experiments, outperforming
240 existing empirical potentials.

241 The high-performance implementation of BFFs, combining accuracy with autonomous
242 uncertainty-driven active learning, opens numerous possibilities to explicitly study dynamics
243 and microscopic mechanisms of phase transformations and non-equilibrium properties such
244 as thermal and ionic transport. The presented unified approach can be extended to a wide
245 range of complex systems and phenomena, where interatomic interactions are difficult to
246 capture with classical approaches while time- and length-scales are out of reach of first-
247 principles computational methods. Uncertainty quantification in MD simulations allows
248 for systematic monitoring of the model confidence and detection of rare and unanticipated
249 phenomena, such as reactions or nucleation of phases. Such events are statistically unlikely

250 to occur in smaller simulations and become increasingly likely and relevant as the simulation
 251 sizes increase, as may be needed to study complex and heterogeneous materials systems.

252 IV. METHODS

253 In this section, we use bold letters such as $\boldsymbol{\alpha}$ and $\boldsymbol{\Lambda}$ to denote a vector or a matrix,
 254 and use indices such as α_i and Λ_{ij} to denote the components of the vector and matrix
 255 respectively. In addition, we use F to represent all the collected configurations with all
 256 atomic environments (the “full” data set), and use S for a subset atomic environments
 257 selected from those configurations (the “sparse” data set).

258 A. Gaussian Process Regression

The local atomic environment ρ_i of an atom i consists of all the neighbor atoms within a cutoff radius, and is associated with a label y_i that can be the force \mathbf{F}_i on atom i or a local energy ε_i . The local energy labels are usually not available in practice, but total energies, stresses and atomic forces are. A kernel function $k(\rho_i, \rho_j)$ quantifies the similarity between two atomic environments, which is also the covariance between local energies. Gaussian process regression (GP) assumes a Gaussian joint distribution of all the training data $\{(\rho_i, y_i)\}$ and test data (ρ, y) . The posterior distribution for test data is also Gaussian with the mean and variance

$$\varepsilon(\rho) = \mathbf{k}_{\varepsilon F}^\top (\mathbf{K}_{FF} + \boldsymbol{\Lambda})^{-1} \mathbf{y} \quad (1)$$

$$V(\rho) = k_{\varepsilon\varepsilon} - \mathbf{k}_{\varepsilon F}^\top (\mathbf{K}_{FF} + \boldsymbol{\Lambda})^{-1} \mathbf{k}_{F\varepsilon} \quad (2)$$

259 Here, ε is the local energy of ρ , $\mathbf{k}_{\varepsilon F}$ is the kernel vector describing covariances between the
 260 test data and all the training data, with element $k(\rho, \rho_i)$, $k_{\varepsilon\varepsilon} = k(\rho, \rho)$ is the kernel between
 261 test data ρ and itself, \mathbf{K}_{FF} is the kernel matrix with element $k(\rho_i, \rho_j)$, $\boldsymbol{\Lambda}$ is a diagonal matrix
 262 describing noise, and \mathbf{y} is the vector of all training labels.

Since the full GP evaluates the kernel between all configurations in the whole training set, it becomes computationally inefficient for large data sets. A sparse approximation is needed such that the computational cost can be reduced while keeping the information as complete as possible. Following our recent work¹⁷ we consider the mean prediction from Deterministic

Training Conditional (DTC) Approximation⁸⁰, and the variance on local energies

$$\varepsilon(\rho) = \mathbf{k}_{\varepsilon S}^\top (\mathbf{K}_{SF} \mathbf{\Lambda}^{-1} \mathbf{K}_{FS} + \mathbf{K}_{SS})^{-1} \mathbf{K}_{SF} \mathbf{y} \quad (3)$$

$$V(\rho) = k_{\varepsilon\varepsilon} - \mathbf{k}_{\varepsilon S} K_{SS}^{-1} \mathbf{k}_{S\varepsilon} \quad (4)$$

where the $\mathbf{k}_{\varepsilon S}$ is the kernel vector between the test data ρ and the sparse training set S , \mathbf{K}_{SF} is the kernel matrix between the sparse subset S and the complete training set F , and \mathbf{K}_{SS} is the kernel matrix between S and itself. The energy, forces and stress tensor of a test configuration are given by the mean prediction, and their corresponding uncertainties are given by the square root of the predictive variance.

B. ACE Descriptors with Inner Product Kernel

In the FLARE SGP formalism¹⁷ we use the atomic cluster expansion⁸¹ (ACE) descriptors to represent the features of a local environment. The total energy is constructed from atomic clusters, represented by the expansion coefficients of an atomic density function using spherical harmonics. We refer the readers to Ref.^{17,81} for more details. To build up the SGP model for interatomic Bayesian force field, or BFF, we use the inner product kernel defined as

$$k(\rho_1, \rho_2) = \sigma^2 \left(\frac{\mathbf{d}_1 \cdot \mathbf{d}_2}{d_1 d_2} \right)^\xi \quad (5)$$

where \mathbf{d}_1 and \mathbf{d}_2 are ACE descriptors of environments ρ_1 and ρ_2 , σ is the signal variance which is optimized by maximizing the log likelihood of SGP, and ξ is the power of the inner product kernel which is selected a priori. We also normalize the kernel by the L2 norm of the descriptors. For simplicity of notations and without loss of generality, we ignore the normalization and only showcase the kernel without derivative associated with energy.

With inner product kernels, a highly efficient but lossless approximation is available via reorganization of the summation in the mathematical expression¹⁷. Defining $\boldsymbol{\alpha} := (\mathbf{K}_{SF} \mathbf{\Lambda}^{-1} \mathbf{K}_{FS} + \mathbf{K}_{SS})^{-1} \mathbf{K}_{SF} \mathbf{y}$ and $\tilde{\mathbf{d}}_i = \mathbf{d}_i / d_i$, the mean prediction of test data ρ_i (Eq.3)

283 from sparse training set $S = \{\rho_s\}$ can be written as¹⁷

$$\begin{aligned}
\varepsilon(\rho_i) &= \sigma^2 \sum_t (\tilde{\mathbf{d}}_i \cdot \tilde{\mathbf{d}}_t)^\xi \alpha_t \\
&= \sigma^2 \sum_{t, m_1, \dots, m_\xi} \tilde{d}_{im_1} \tilde{d}_{tm_1} \cdots \tilde{d}_{im_\xi} \tilde{d}_{tm_\xi} \alpha_t \\
&= \sigma^2 \sum_{m_1, \dots, m_\xi} \tilde{d}_{im_1} \cdots \tilde{d}_{im_\xi} \left(\sum_t \tilde{d}_{tm_1} \cdots \tilde{d}_{tm_\xi} \alpha_t \right) \\
&= \sum_{m_1, \dots, m_\xi} \tilde{d}_{im_1} \cdots \tilde{d}_{im_\xi} \beta_{m_1, \dots, m_\xi},
\end{aligned} \tag{6}$$

284 The β tensor can be computed from the training data descriptors. Thus, we can store the
285 β tensor, and during the prediction we directly evaluate Eq. 6 without the need to sum over
286 all training data t .

287 Crucially, the variance Eq. 4 has the similar reorganization as the mean prediction of
288 Eq. 6

$$V(\rho_i) = \sigma^2 (\tilde{\mathbf{d}}_i \cdot \tilde{\mathbf{d}}_i)^\xi - \sigma^4 \sum_{s, t} (\tilde{\mathbf{d}}_i \cdot \tilde{\mathbf{d}}_s)^\xi (K_{SS}^{-1})_{st} (\tilde{\mathbf{d}}_t \cdot \tilde{\mathbf{d}}_i)^\xi \tag{7}$$

$$= \sum_{\substack{m_1, \dots, m_\xi \\ n_1, \dots, n_\xi}} (\tilde{d}_{im_1} \cdots \tilde{d}_{im_\xi}) \gamma_{n_1, \dots, n_\xi}^{m_1, \dots, m_\xi} (\tilde{d}_{in_1} \cdots \tilde{d}_{in_\xi}) \tag{8}$$

289 where γ is a tensor that can be calculated and stored once the training data is collected,
290 and used in inference without explicit summation over training data i .

291 The reorganization indicates that the SGP regression with inner product kernel essentially
292 gives a polynomial model of the descriptors. Denote n_d as the descriptor dimension. The
293 reorganized mean prediction has both the β size and the computational cost as $O(n_d^\xi)$.
294 While the reorganized variance prediction has both the γ size and the computational cost as
295 $O(n_d^{2\xi})$. By the reorganization, both the mean and variance predictions become independent
296 of the training set and get rid of the linear scaling with respect to training size. Here, we
297 choose $\xi = 2$ for the mean prediction, because 1) it is shown¹⁷ that $\xi = 2$ has a significant
298 improvement of likelihood compared to $\xi = 1$, while the improvement of $\xi > 2$ is marginal;
299 and 2) higher order requires a much larger memory for β tensor, and the evaluation of Eq.6
300 is much costlier than $\xi = 2$.

301 From Eq.8 we see that the variance has twice the polynomial degree of that for the mean
302 prediction. For example, when $\xi = 2$, the mean prediction is a quadratic model while the

303 variance is a quartic model of descriptors. For computational efficiency, in this work we use
304 $V_{\xi=1}$ for variance prediction. $V_{\xi=1}$ is not the exact variance of our mean prediction $\varepsilon_{\xi=2}$,
305 but an approximation using the same hyperparameters as $V_{\xi=2}$. It has a strong correlation
306 with the exact variance $V_{\xi=2}$ as shown in Fig.S1 of supplementary materials⁶². Especially,
307 the correlation coefficients between $V_{\xi=1}$ and higher powers are close to 1.0, the perfect
308 linear relation, even with a training size of 200 frames. This indicates that uncertainty
309 quantification with $V_{\xi=1}$ is able to recognize discrepancies between different configurations
310 as well as $V_{\xi=2}$. Specifically, atomic environments with higher $V_{\xi=2}$ uncertainties will also
311 be assigned higher $V_{\xi=1}$ uncertainties than others. It is then justified that $V_{\xi=1}$ can be used
312 as a strongly correlated but much cheaper approximation of $V_{\xi=2}$.

313 To summarize, we use $\varepsilon_{\xi=2}$ and $V_{\xi=1}$ for mean and variance predictions respectively,
314 where both are quadratic models with respect to the descriptors. During the on-the-fly
315 active learning, every time the training set is updated by the new DFT data, the β and
316 γ matrices are computed from training data descriptors and stored as coefficient files. In
317 LAMMPS MD, the quadratic models are evaluated to make predictions for energy, forces,
318 stress and uncertainty of the configurations.

319 V. CODE & DATA AVAILABILITY

320 The code for FLARE BFF and BAL is available at [https://github.com/mir-group/](https://github.com/mir-group/flare)
321 `flare`.

322 The scripts and data are available in Zenodo: [https://doi.org/10.5281/zenodo.](https://doi.org/10.5281/zenodo.5797177)
323 `5797177`.

324 VI. ACKNOWLEDGEMENT

325 We thank Lixin Sun, Thomas Eckl, Matous Mrovec, Thomas Hammerschmidt and Ralf
326 Drautz for helpful discussions on the construction of the force field and properties of SiC.
327 We thank Jenny Coulter and Andrea Cepellotti for the helpful instructions on thermal
328 conductivity calculation using Phono3py and Phoebe. We thank Jenny Hoffman, Sushmita
329 Bhattacharya and Kristina Jacobsson for constructive suggestions on the manuscript. We
330 acknowledge support from the US Department of Energy (DOE), Office of Science, Office

331 of Basic Energy Sciences (BES) under Award No. DE-SC0020128, and the National Science
332 Foundation through the Harvard University Materials Research Science and Engineering
333 Center DMR-2011754 and Grant No. 2003725, Robert Bosch LLC and Aker scholarship.
334 Computations were performed on the FASRC Cannon cluster supported by the Research
335 Computing Group at Harvard University.

336 VII. AUTHOR CONTRIBUTIONS

337 J.V., Y.X. and A.J. developed the FLARE code, the corresponding LAMMPS pair styles
338 and compute commands. Y.X. implemented the on-the-fly training workflow coupled with
339 LAMMPS. Y.X. performed the on-the-fly training and MD simulation of SiC. S.R. performed
340 DFT calculations of SiC polymorphs. Y.X. computed the thermal conductivity of SiC with
341 the contribution of N.H.P. B.K. conceived the application and supervised the work. Y.X.
342 and B.K. wrote the manuscript. All authors contributed to manuscript preparation.

343 VIII. COMPETING INTERESTS

344 The authors declare no competing financial or non-financial interests.

345 * xiey@g.harvard.edu

346 † bkoz@seas.harvard.edu

347 ¹ Jörg Behler and Michele Parrinello. Generalized neural-network representation of high-
348 dimensional potential-energy surfaces. Phys. Rev. Lett., 98(14):146401, 2007.

349 ² Alexander V Shapeev. Moment tensor potentials: A class of systematically improvable inter-
350 atomic potentials. Multiscale Modeling & Simulation, 14(3):1153–1173, 2016.

351 ³ Aidan Patrick Thompson, Laura Pailton Swiler, Christian Robert Trott, Stephen Martin Foiles,
352 and Garritt J. Tucker. Snap: Automated generation of quantum-accurate interatomic potentials.
353 J. Comput. Phys., 9 2014.

354 ⁴ Kristof Schütt, Pieter-Jan Kindermans, Huziel Enoc Saucedo Felix, Stefan Chmiela, Alexandre
355 Tkatchenko, and Klaus-Robert Müller. Schnet: A continuous-filter convolutional neural network

356 for modeling quantum interactions. In Advances in Neural Information Processing Systems,
357 pages 991–1001, 2017.

358 ⁵ Albert P Bartók, Mike C Payne, Risi Kondor, and Gábor Csányi. Gaussian approximation
359 potentials: The accuracy of quantum mechanics, without the electrons. Phys. Rev. Lett.,
360 104(13):136403, 2010.

361 ⁶ Jonathan Vandermause, Steven B Torrisi, Simon Batzner, Yu Xie, Lixin Sun, Alexie M Kolpak,
362 and Boris Kozinsky. On-the-fly active learning of interpretable bayesian force fields for atomistic
363 rare events. npj Comput. Mater., 6(1):1–11, 2020.

364 ⁷ Simon Batzner, Tess E Smidt, Lixin Sun, Jonathan P Mailoa, Mordechai Kornbluth, Nicola
365 Molinari, and Boris Kozinsky. Se (3)-equivariant graph neural networks for data-efficient and
366 accurate interatomic potentials. Preprint at <https://arxiv.org/abs/2101.03164>, 2021.

367 ⁸ Ryosuke Jinnouchi, Jonathan Lahnsteiner, Ferenc Karsai, Georg Kresse, and Menno Bokdam.
368 Phase transitions of hybrid perovskites simulated by machine-learning force fields trained on
369 the fly with bayesian inference. Physical review letters, 122(22):225701, 2019.

370 ⁹ Ryosuke Jinnouchi, Ferenc Karsai, and Georg Kresse. On-the-fly machine learning force field
371 generation: Application to melting points. Physical Review B, 100(1):014105, 2019.

372 ¹⁰ Zhenwei Li, James R Kermode, and Alessandro De Vita. Molecular dynamics with on-the-fly
373 machine learning of quantum-mechanical forces. Physical review letters, 114(9):096405, 2015.

374 ¹¹ Evgeny V Podryabinkin and Alexander V Shapeev. Active learning of linearly parametrized
375 interatomic potentials. Computational Materials Science, 140:171–180, 2017.

376 ¹² M Hodapp and A Shapeev. In operando active learning of interatomic interaction during large-
377 scale simulations. Mach. Learn.: Sci. Technol., 1(4):045005, sep 2020.

378 ¹³ Tom Young, Tristan Johnston-Wood, Volker L. Deringer, and Fernanda Duarte. A transferable
379 active-learning strategy for reactive molecular force fields. Chem. Sci., pages –, 2021.

380 ¹⁴ Aldo Glielmo, Claudio Zeni, and Alessandro De Vita. Efficient nonparametric n-body force
381 fields from machine learning. Phys. Rev. B, 97(18):184307, 2018.

382 ¹⁵ Aldo Glielmo, Claudio Zeni, Ádám Fekete, and Alessandro De Vita. Building nonparametric
383 n-body force fields using gaussian process regression. In Machine Learning Meets Quantum
384 Physics, pages 67–98. Springer, 2020.

385 ¹⁶ Yu Xie, Jonathan Vandermause, Lixin Sun, Andrea Cepellotti, and Boris Kozinsky. Bayesian
386 force fields from active learning for simulation of inter-dimensional transformation of stanene.

- 387 [npj Computational Materials](#), 7(1):1–10, 2021.
- 388 ¹⁷ Jonathan Vandermause, Yu Xie, Jin Soo Lim, Cameron J. Owen, and Boris Kozinsky. Ac-
389 tive learning of reactive bayesian force fields: Application to heterogeneous hydrogen-platinum
390 catalysis dynamics, 2021.
- 391 ¹⁸ Steve Plimpton. Fast parallel algorithms for short-range molecular dynamics. [Journal of](#)
392 [computational physics](#), 117(1):1–19, 1995.
- 393 ¹⁹ S. Castelletto, B. C. Johnson, V. Ivády, N. Stavrias, T. Umeda, A. Gali, and T. Ohshima. A
394 silicon carbide room-temperature single-photon source. [Nature Materials](#), 13(2), 2014.
- 395 ²⁰ Matthias Widmann, Sang-Yun Lee, Torsten Rendler, Nguyen Tien Son, Helmut Fedder, Seoy-
396 oung Paik, Li-Ping Yang, Nan Zhao, Sen Yang, Ian Booker, Andrej Denisenko, Mohammad
397 Jamali, S Ali Momenzadeh, Ilja Gerhardt, Takeshi Ohshima, Adam Gali, Erik Janzén, and Jörg
398 Wrachtrup. Coherent control of single spins in silicon carbide at room temperature. [Nature](#)
399 [Materials](#), 14(2):164–168, 2015.
- 400 ²¹ Roland Nagy, Matthias Niethammer, Matthias Widmann, Yu-Chen Chen, Péter Udvarhelyi,
401 Cristian Bonato, Jawad Ul Hassan, Robin Karhu, Ivan G Ivanov, Nguyen Tien Son, Jeronimo R
402 Maze, Takeshi Ohshima, Öney O Soykal, Ádám Gali, Sang-Yun Lee, Florian Kaiser, and Jörg
403 Wrachtrup. High-fidelity spin and optical control of single silicon-vacancy centres in silicon
404 carbide. [Nature Communications](#), 10(1), dec 2019.
- 405 ²² Abram L. Falk, Paul V. Klimov, Bob B. Buckley, Viktor Ivády, Igor A. Abrikosov, Greg Calu-
406 sine, William F. Koehl, Ádám Gali, and David D. Awschalom. Electrically and mechanically
407 tunable electron spins in silicon carbide color centers. [Phys. Rev. Lett.](#), 112:187601, May 2014.
- 408 ²³ David J. Christle, Paul V. Klimov, Charles F. de las Casas, Krisztián Szász, Viktor Ivády,
409 Valdas Jokubavicius, Jawad Ul Hassan, Mikael Syväjärvi, William F. Koehl, Takeshi Ohshima,
410 Nguyen T. Son, Erik Janzén, Ádám Gali, and David D. Awschalom. Isolated spin qubits in sic
411 with a high-fidelity infrared spin-to-photon interface. [Phys. Rev. X](#), 7:021046, Jun 2017.
- 412 ²⁴ Gang Zhang, Yuan Cheng, Jyh-Pin Chou, and Adam Gali. Material platforms for defect qubits
413 and single-photon emitters. [Applied Physics Reviews](#), 7(3):031308, 2020.
- 414 ²⁵ Stefania Castelletto and Alberto Boretti. Silicon carbide color centers for quantum applications.
415 [Journal of Physics: Photonics](#), 2(2):022001, 2020.
- 416 ²⁶ Samuel J Whiteley, Gary Wolfowicz, Christopher P Anderson, Alexandre Bourassa, He Ma,
417 Meng Ye, Gerwin Koolstra, Kevin J Satzinger, Martin V Holt, F Joseph Heremans, et al.

- 418 Spin-phonon interactions in silicon carbide addressed by gaussian acoustics. Nature Physics,
419 15(5):490–495, 2019.
- 420 ²⁷ Lixin Sun, Chune Lan, Shijun Zhao, Jianming Xue, and Yugang Wang. Self-irradiation of thin
421 sic nanowires with low-energy ions: a molecular dynamics study. Journal of Physics D: Applied
422 Physics, 45:135403, 4 2012.
- 423 ²⁸ Yanwen Zhang, G Malcolm Stocks, Ke Jin, Chenyang Lu, Hongbin Bei, Brian C Sales, Lumin
424 Wang, Laurent K Béland, Roger E Stoller, German D Samolyuk, et al. Influence of chemical
425 disorder on energy dissipation and defect evolution in concentrated solid solution alloys. Nature
426 communications, 6(1):1–9, 2015.
- 427 ²⁹ Yanwen Zhang, Ritesh Sachan, Olli H Pakarinen, Matthew F Chisholm, Peng Liu, Haizhou Xue,
428 and William J Weber. Ionization-induced annealing of pre-existing defects in silicon carbide.
429 Nature communications, 6(1):1–7, 2015.
- 430 ³⁰ R. Devanathan, F. Gao, and W. J. Weber. Molecular dynamics simulation of point defect
431 accumulation in 3c-sic. Materials Research Society Symposium - Proceedings, 792, 2003.
- 432 ³¹ Rodrick Kuate Defo, Xingyu Zhang, David Bracher, Gunn Kim, Evelyn Hu, and Efthimios
433 Kaxiras. Energetics and kinetics of vacancy defects in 4h-sic. Physical Review B, 98, 9 2018.
- 434 ³² Francesca Miozzi, Guillaume Morard, Daniele Antonangeli, Alisha N Clark, Mohamed Mezouar,
435 Caroline Dorn, A Rozel, and Guillaume Fiquet. Equation of state of sic at extreme condi-
436 tions: New insight into the interior of carbon-rich exoplanets. Journal of Geophysical Research:
437 Planets, 123(9):2295–2309, 2018.
- 438 ³³ Valery I Levitas, Yanzhang Ma, Emre Selvi, Jianzhe Wu, and John A Patten. High-density
439 amorphous phase of silicon carbide obtained under large plastic shear and high pressure. Physical
440 Review B, 85(5):054114, 2012.
- 441 ³⁴ SJ Tracy, RF Smith, JK Wicks, DE Fratanduono, AE Gleason, CA Bolme, VB Prakapenka,
442 S Speziale, Karen Appel, A Fernandez-Pañella, et al. In situ observation of a phase transition
443 in silicon carbide under shock compression using pulsed x-ray diffraction. Physical Review B,
444 99(21):214106, 2019.
- 445 ³⁵ T Sekine and T Kobayashi. Shock compression of 6h polytype sic to 160 gpa. Physical Review
446 B, 55(13):8034, 1997.
- 447 ³⁶ TJ Vogler, WD Reinhart, LC Chhabildas, and DP Dandekar. Hugoniot and strength behavior
448 of silicon carbide. Journal of applied physics, 99(2):023512, 2006.

- 449 ³⁷ Minoru Yoshida, Akifumi Onodera, Masaki Ueno, Kenichi Takemura, and Osamu Shimomura.
450 Pressure-induced phase transition in sic. Physical Review B, 48(14):10587, 1993.
- 451 ³⁸ Yuto Kidokoro, Koichiro Umamoto, Kei Hirose, and Yasuo Ohishi. Phase transition in sic from
452 zinc-blende to rock-salt structure and implications for carbon-rich extrasolar planets. American
453 Mineralogist: Journal of Earth and Planetary Materials, 102(11):2230–2234, 2017.
- 454 ³⁹ Kierstin Daviau and Kanani KM Lee. Zinc-blende to rocksalt transition in sic in a laser-heated
455 diamond-anvil cell. Physical Review B, 95(13):134108, 2017.
- 456 ⁴⁰ Cheng-Zhang Wang, Rici Yu, and Henry Krakauer. Pressure dependence of born effective
457 charges, dielectric constant, and lattice dynamics in sic. Physical Review B, 53(9):5430, 1996.
- 458 ⁴¹ Zheng Ran, Chunming Zou, Zunjie Wei, Hongwei Wang, Rong Zhang, and Ning Fang.
459 Phase transitions and elastic anisotropies of sic polymorphs under high pressure. Ceramics
460 International, 47(5):6187–6200, 2021.
- 461 ⁴² WH Lee and XH Yao. First principle investigation of phase transition and thermodynamic
462 properties of sic. Computational Materials Science, 106:76–82, 2015.
- 463 ⁴³ Murat Durandurdu. Pressure-induced phase transition of sic. Journal of Physics: Condensed
464 Matter, 16(25):4411, 2004.
- 465 ⁴⁴ Yu-Ping Lu, Duan-Wei He, Jun Zhu, and Xiang-Dong Yang. First-principles study of pressure-
466 induced phase transition in silicon carbide. Physica B: Condensed Matter, 403(19-20):3543–
467 3546, 2008.
- 468 ⁴⁵ HY Xiao, Fei Gao, Xiaotao T Zu, and William J Weber. Ab initio molecular dynamics simu-
469 lation of a pressure induced zinc blende to rocksalt phase transition in sic. Journal of Physics:
470 Condensed Matter, 21(24):245801, 2009.
- 471 ⁴⁶ S Gorai, C Bhattacharya, and G Kondayya. Pressure induced structural phase transition in sic.
472 In AIP Conference Proceedings, volume 1832, page 030010. AIP Publishing LLC, 2017.
- 473 ⁴⁷ Tavneet Kaur and MM Sinha. First principle study of structural, electronic and vibrational
474 properties of 3c-sic. In AIP Conference Proceedings, volume 2265, page 030384. AIP Publishing
475 LLC, 2020.
- 476 ⁴⁸ J. Tersoff. Chemical order in amorphous silicon carbide. Physical Review B, 49(23):16349, 1994.
- 477 ⁴⁹ Paul Erhart and Karsten Albe. Analytical potential for atomistic simulations of silicon, carbon,
478 and silicon carbide. Physical Review B, 71(3), January 2005.

- 479 ⁵⁰ Fuyuki Shimojo, Ingvar Ebbsjö, Rajiv K Kalia, Aiichiro Nakano, Jose P Rino, and Priya
480 Vashishta. Molecular dynamics simulation of structural transformation in silicon carbide under
481 pressure. Physical review letters, 84(15):3338, 2000.
- 482 ⁵¹ Priya Vashishta, Rajiv K. Kalia, Aiichiro Nakano, and José Pedro Rino. Interaction potential
483 for silicon carbide: A molecular dynamics study of elastic constants and vibrational density of
484 states for crystalline and amorphous silicon carbide. Journal of Applied Physics, 101(10):103515,
485 May 2007.
- 486 ⁵² Kyung-Han Kang, Taihee Eun, Myong-Chul Jun, and Byeong-Joo Lee. Governing factors for
487 the formation of 4h or 6h-SiC polytype during SiC crystal growth: An atomistic computational
488 approach. Journal of Crystal Growth, 389:120–133, March 2014.
- 489 ⁵³ Fei Gao and William J. Weber. Empirical potential approach for defect properties in 3c-
490 SiC. Nuclear Instruments and Methods in Physics Research Section B: Beam Interactions
491 with Materials and Atoms, 191(1-4):504–508, 2002.
- 492 ⁵⁴ Chris M Handley, Glenn I Hawe, Douglas B Kell, and Paul LA Popelier. Optimal construction of
493 a fast and accurate polarisable water potential based on multipole moments trained by machine
494 learning. Physical Chemistry Chemical Physics, 11(30):6365–6376, 2009.
- 495 ⁵⁵ Albert P Bartók, James Kermode, Noam Bernstein, and Gábor Csányi. Machine learning a
496 general-purpose interatomic potential for silicon. Physical Review X, 8(4):041048, 2018.
- 497 ⁵⁶ Linfeng Zhang, Jiequn Han, Han Wang, Roberto Car, and E Weinan. Deep potential molec-
498 ular dynamics: a scalable model with the accuracy of quantum mechanics. Phys. Rev. Lett.,
499 120(14):143001, 2018.
- 500 ⁵⁷ Jonathan P Mailoa, Mordechai Kornbluth, Simon Batzner, Georgy Samsonidze, Stephen T
501 Lam, Jonathan Vandermause, Chris Ablitt, Nicola Molinari, and Boris Kozinsky. A fast neu-
502 ral network approach for direct covariant forces prediction in complex multi-element extended
503 systems. Nature machine intelligence, 1(10):471–479, 2019.
- 504 ⁵⁸ Wei Chen and Liang-Sheng Li. The study of the optical phonon frequency of 3c-sic by molec-
505 ular dynamics simulations with deep neural network potential. Journal of Applied Physics,
506 129(24):244104, 2021.
- 507 ⁵⁹ Baoqin Fu, Yandong Sun, Linfeng Zhang, Han Wang, and Ben Xu. Deep learning inter-atomic
508 potential for thermal and phonon behaviour of silicon carbide with quantum accuracy. arXiv
509 preprint arXiv:2110.10843, 2021.

- 510 ⁶⁰ Senja Ramakers, Anika Marusczyk, Maximilian Amsler, Thomas Eckl, Matous Mrovec, Thomas
511 Hammerschmidt, and Ralf Drautz. Effects of thermal, elastic and surface properties on the
512 stability of sic polytypes, 2022.
- 513 ⁶¹ Federico A Soria, Weiwei Zhang, Patricia A Paredes-Olivera, Adri CT Van Duin, and Eduardo M
514 Patrito. Si/c/h reaxff reactive potential for silicon surfaces grafted with organic molecules. The
515 Journal of Physical Chemistry C, 122(41):23515–23527, 2018.
- 516 ⁶² Yu Xie, Jonathan Vandermause, Senja Ramakers, Nakib H. Protik, Anders Johansson, and
517 Boris Kozinsky. Supplementary materials. 2022.
- 518 ⁶³ G Lucas, M Bertolus, and L Pizzagalli. An environment-dependent interatomic potential for
519 silicon carbide: calculation of bulk properties, high-pressure phases, point and extended defects,
520 and amorphous structures. Journal of Physics: Condensed Matter, 22(3):035802, 2009.
- 521 ⁶⁴ Peter Mahler Larsen, Søren Schmidt, and Jakob Schiøtz. Robust structural identification via
522 polyhedral template matching. Modelling and Simulation in Materials Science and Engineering,
523 24(5):055007, 2016.
- 524 ⁶⁵ Alexander Stukowski. Visualization and analysis of atomistic simulation data with ovito–
525 the open visualization tool. Modelling and Simulation in Materials Science and Engineering,
526 18(1):015012, 2009.
- 527 ⁶⁶ A Togo and I Tanaka. First principles phonon calculations in materials science. Scr. Mater.,
528 108:1–5, Nov 2015.
- 529 ⁶⁷ Stanislaw Nowak. Crystal lattice dynamics of various silicon-carbide polytypes. In International
530 Conference on Solid State Crystals 2000: Growth, Characterization, and Applications of Single
531 Crystals, volume 4412, pages 181–186. International Society for Optics and Photonics, 2001.
- 532 ⁶⁸ D. W. Feldman, James H. Parker, W. J. Choyke, and Lyle Patrick. Phonon Dispersion Curves
533 by Raman Scattering in SiC, Polytypes 3 C , 4 H , 6 H , 1 5 R , and 2 1 R. Physical Review,
534 173(3):787–793, September 1968.
- 535 ⁶⁹ Shin-ichi Nakashima, Atsuo Wada, and Zenzaburo Inoue. Raman scattering from anisotropic
536 phonon modes in sic polytypes. Journal of the Physical Society of Japan, 56(9):3375–3380,
537 1987.
- 538 ⁷⁰ J Serrano, J Stremper, M Cardona, M Schwoerer-Böhning, H Requardt, M Lorenzen, B Stojetz,
539 P Pavone, and WJ Choyke. Determination of the phonon dispersion of zinc blende (3c) silicon
540 carbide by inelastic x-ray scattering. Applied physics letters, 80(23):4360–4362, 2002.

- 541 ⁷¹ Robert M Pick, Morrel H Cohen, and Richard M Martin. Microscopic theory of force constants
542 in the adiabatic approximation. Physical Review B, 1(2):910, 1970.
- 543 ⁷² Nakib Haider Protik, Ankita Katre, Lucas Lindsay, Jesús Carrete, Natalio Mingo, and David
544 Broido. Phonon thermal transport in 2h, 4h and 6h silicon carbide from first principles. Materials
545 Today Physics, 1:31–38, June 2017.
- 546 ⁷³ Atsushi Togo, Laurent Chaput, and Isao Tanaka. Distributions of phonon lifetimes in brillouin
547 zones. Phys. Rev. B, 91:094306, Mar 2015.
- 548 ⁷⁴ Andrea Cepellotti, Jennifer Coulter, Anders Johansson, Natalya S Fedorova, and Boris Kozin-
549 sky. Phoebe: a collection of phonon and electron boltzmann equation solvers. arXiv preprint
550 arXiv:2111.14999, 2021.
- 551 ⁷⁵ M Omini and A Sparavigna. An iterative approach to the phonon boltzmann equation in the
552 theory of thermal conductivity. Physica B: Condensed Matter, 212(2):101–112, 1995.
- 553 ⁷⁶ RE Taylor, H Groot, and J Ferrier. Thermophysical properties of cvd sic. TRPL1336,
554 Thermophysical Properties Research Laboratory Report, School of Mechanical Engineering,
555 Purdue University, 1993.
- 556 ⁷⁷ DJ Senior, DJ Trimble, GE Youngblood, GA Newsome, CE Moore, and JJ Woods. Effects of
557 neutron irradiation on thermal conductivity of sic-based composites and monolithic ceramics.
558 Fusion Technology, 30(3P2A):943–955, 1996.
- 559 ⁷⁸ D Morelli, J Heremans, C Beetz, WS Woo, G Harris, and C Taylor. Carrier concentration
560 dependence of the thermal conductivity of silicon carbide. In Institute of Physics Conference
561 Series, volume 137, pages 313–316. Bristol [England]; Boston: Adam Hilger, Ltd., c1985-, 1994.
- 562 ⁷⁹ JE Graebner, H Altmann, NM Balzaretta, R Campbell, H-B Chae, A Degiovanni, R Enck,
563 A Feldman, D Fournier, J Fricke, et al. Report on a second round robin measurement of the
564 thermal conductivity of cvd diamond. Diamond and Related materials, 7(11-12):1589–1604,
565 1998.
- 566 ⁸⁰ Joaquin Quinonero-Candela and Carl Edward Rasmussen. A unifying view of sparse approx-
567 imate gaussian process regression. The Journal of Machine Learning Research, 6:1939–1959,
568 2005.
- 569 ⁸¹ Ralf Drautz. Atomic cluster expansion for accurate and transferable interatomic potentials.
570 Physical Review B, 99(1), January 2019.

Supplementary Files

This is a list of supplementary files associated with this preprint. Click to download.

- [SI.pdf](#)